Geometrical properties of avalanches in self-organized critical models of solar flares

Scott W. McIntosh*
ESA Space Science Department, NASA/GSFC, Mailcode 682.3, Greenbelt, Maryland 20771

Paul Charbonneau, Thomas J. Bogdan, Han-Li Liu, and James P. Norman†
High Altitude Observatory, National Center for Atmospheric Research, P.O. Box 3000, Boulder, Colorado 80307
(Received 26 October 2001; published 4 April 2002)

We investigate the geometrical properties of avalanches in self-organized critical models of solar flares. Traditionally, such models differ from the classical sandpile model in their formulation of stability criteria in terms of the curvature of the nodal field, and belong to a distinct universality class. With a view toward comparing these properties to those inferred from spatially and temporally resolved flare observations, we consider the properties of avalanche peak snapshots, time-integrated avalanches in two and three dimensions, and the two-dimensional projections of the latter. The nature of the relationship between the avalanching volume and its projected area is an issue of particular interest in the solar flare context. Using our simulation results we investigate this relationship, and demonstrate that proper accounting of the fractal nature of avalanches can bring into agreement hitherto discrepant results of observational analyses based on simple, nonfractal geometries for the flaring volume.

DOI: 10.1103/PhysRevE.65.046125 PACS number(s): 05.65.+b, 95.30.Qd, 45.70.Cc, 52.35.Vd

I. INTRODUCTION

Solar flares are the observational manifestation of sudden, spatially localized energy release in the solar atmosphere. In a matter of a few seconds the local coronal temperature can increase to as high as a few 10^7 K from its average ambient value of $\sim 10^6$ K, before thermal relaxation sets in. Flaring is accompanied by a rapid increase of emission at most wavelengths of the electromagnetic spectrum, but is most spectacular—and readily observed—at short wavelength ($\leqslant$2000 Å), corresponding to the ultraviolet (uv), extreme-ultraviolet (euv), and x-ray regions of the spectrum.

It is now generally agreed that the flare energy source comes from the local reconfiguration of the solar coronal magnetic field, with the larger flares originating in regions of strongest fields, such as those overlying sunspots and active regions. In the high electrical conductivity environment of the solar outer atmosphere and corona, the most viable fast reconfiguration mechanism is magnetic reconnection. In its simplest form, reconnection sets in when magnetic fields of opposite polarities are forced together to form a thin electric current sheet, with the current growing in strength until plasma instabilities cause a rapid increase in the resistivity of the plasma. This, in turn, leads to local dissipation and topological reconfiguration of the magnetic field in the vicinity of the current sheet (see [1], Chap. 11).

Flaring has potentially profound implications for coronal heating. It is now generally accepted that the mechanical energy associated with bulk fluid motions in the solar photosphere is, ultimately, the source tapped into by the Sun to heat its corona. However, nothing resembling a consensus currently exists as to the nature of the physical mechanism(s) responsible for the conversion of this mechanical energy into the thermal energy of the coronal plasma. Since magnetic fields are ubiquitous throughout the Sun's outer atmosphere, the magnetic energy dissipated in reconnection-mediated flaring events can, in principle, provide a heating source.[1] Estimates of chromospheric and coronal energy losses place the required average energy deposition rate at about 10^7 erg cm^{-2} s^{-1} [2]. This then raises two related questions: (1) are flares frequent and energetic enough to meet this demand? and (2) how is photospheric mechanical energy converted and stored as available magnetic energy in preflare coronal structures?

Great progress has been made over the years in attempting to answer the first of these two questions. Observations of solar flares by space-borne instruments have gone from spatially unresolved ''Sun as a Star'' observations, e.g., from the Solar Maximum Mission Hard X-Ray Burst Spectrometer (SMM HXRBS [3]) to those of the Solar and Heliospheric Observatory (SOHO [4]) Extreme-Ultraviolet Imaging Telescope (EIT [5]) and the high spatial resolution Transition Region and Coronal Explorer (TRACE [6]) telescope. Analysis of the many hundreds of thousands of flares that have been recorded by these various instruments, of which Fig. 1 gives an example, have revealed the remarkable fact that the frequency distribution of the energy released by flares has the form of a tight power law, spanning at least eight decades in flare energy. Specifically, if $f(E)dE$ is the number per unit time of flares dissipating an amount of en-

*Corresponding author.
Electronic address: scott@esa.nascom.nasa.gov
†Present address: Physics Department, University of Newcastle upon Tyne, Newcastle upon Tyne, NE1 7RU, United Kingdom.

[1]More specifically, the strong electrical fields generated by magnetic reconnection accelerate to superthermal velocities charged particles located in and around the reconnection site; these fast particles then collisionally transfer their energy to other neighboring particles, thus leading to heating of the plasma surrounding the reconnection site.

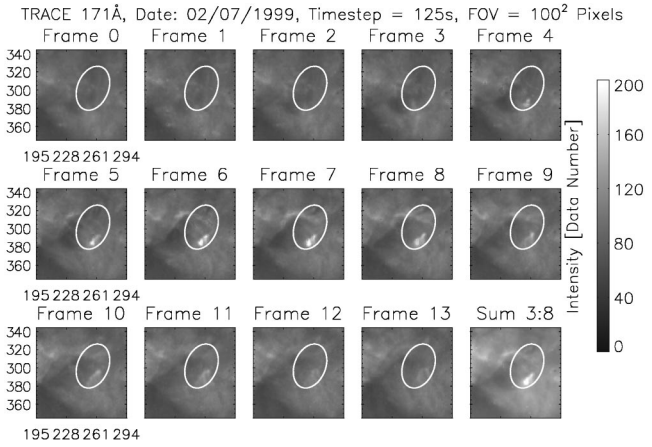

FIG. 1. The temporal evolution of a small flare as observed in euv by TRACE. This flare was studied in detail in [2,3]. The flaring pixels are assumed to lie within an ellipse corresponding to the projection of a loop onto the plane of the sky. The size and orientation of this ellipse are adjusted in order to enclose all pixels that show a significant variation ($\geqslant 3$ standard deviations above background) over the duration of the nanoflare, as shown on each panel. Successive frames are taken 125 s apart and each shows an area of 100 pixels^2 (or $\sim$ 50^2 arc s). To get a better appreciation for the range of euv nanoflaring morphologies, see also Fig. 2 of [3].

ergy in the range E to $E+dE$, then flare data are well described by

$$f(E)dE = f_0 E^{-\alpha_E} dE \ \ \mathrm{s}^{-1} \qquad (\alpha_E > 0). \tag{1}$$

Taking Eq. (1) at face value, the total energy per unit time released collectively by the ensemble of solar flares is then

$$\frac{dE_{tot}}{dt} = \int_{E_{min}}^{E_{max}} f(E) E dE = f_0 \left[\frac{E^{2-\alpha_E}}{2-\alpha_E} \right]_{E_{min}}^{E_{max}} \ \ \mathrm{erg\ s}^{-1}$$

$$(\alpha_E \neq 2) \tag{2}$$

with $E_{max} \sim 10^{33}$ erg, and $E_{min} \sim 10^{24}$ erg for current uv-euv detection limits [7]. If $\alpha_E < 2$ then the largest flares will dominate the energy budget; conversely, if $\alpha_E > 2$ the smaller flares dominate. Observationally, large flares ($E > 10^{32}$ erg, say) are hard to miss, and it is now well established that they are too infrequent to heat the corona, even at epochs of maximum solar activity (see, e.g., [8]).

For close to two decades, Parker has championed the view that coronal heating occurs via numerous small scale reconnection events, which he termed ''nanoflares'' because his estimate of their total energy release falls about nine orders of magnitude below that of large flares [9–11]. Parker's physical picture of how this takes place also happens to address the second question raised above; namely, the conversion of photospheric mechanical energy to magnetic energy in preflare coronal structures. Consider a magnetic structure embedded in the solar corona, for example, a coronal loop. The loop is anchored in the dense plasma of the solar photosphere, where its footpoints are subjected to random horizontal fluid motions associated with the photospheric manifestations of convection and granulation. At photospheric levels the energy density of the plasma greatly exceeds that of the magnetic field, so that field lines cannot resist the motion of the electrically conducting fluid, and consequently are shuffled around as they each execute a form of random walk. The resulting twisting and braiding propagates upward in the form of low frequency Alfvén waves, perturbing the dynamical balance of the overlying magnetic structure. In the corona it is now the energy density of the magnetic field that largely exceeds that of the plasma, so that the field tends to rapidly readjust to a force-free state. However, the high electrical conductivity of the coronal plasma means that the field is ''frozen in'' and the topology of the magnetic structure cannot change. As a result, the field will relax to a state that is force-free everywhere except in a large number of small electrical current sheets building up in regions where field lines are twisted or braided around one another. As photospheric fluid motions inexorably increase this twisting and braiding, the electrical currents build up to the point where the onset of magnetic reconnection becomes inevitable, locally releasing energy in the corona. Parker goes on to speculate that the observed x-ray corona is nothing more than the collective effect of a large number of such nanoflares continuously occurring throughout the magnetized corona.

In this picture, the coronal magnetic field thus acts both as an upward transport mechanism and as an intermediate energy storage medium for the mechanical energy of photospheric fluid motions, and magnetic reconnection is responsible for converting this stored magnetic energy into thermal energy within the coronal plasma. Although not originally emphasized by Parker, the magnetic field reconfiguration taking place in the vicinity of reconnecting current sheet will alter the physical conditions around neighboring current sheets, which may trigger further reconnection events at some of these sheets, and so on, leading to an avalanche of reconnection events cascading throughout the tangled magnetic structure. The associated collective energy release can then be interpreted as a large flare. Moreover, the self-similarity typically associated with such avalanche processes provides a natural interpretation for the observed power law in flare size. Parker's model in fact includes all the ingredients deemed necessary to lead to self-organized criticality (SOC; [12–14]): a slowly driven (photospheric footpoint motions) open system (magnetic structure embedded in the solar corona) subject to a self-stabilizing local threshold instability (magnetic reconnection) leading to localized transport and readjustment of the physical quantity subject to instability [14–16].

Clearly, Parker's conjecture of coronal heating by nanoflares requires $\alpha_E > 2$ in Eq. (1). At the present time, this is neither convincingly supported nor refuted by extant observational analyses, which place α_E anywhere in the range 1.5–2.6 (see [16], and references therein). Whether nanoflares heat the corona or not, Parker's picture still provides a sound physical underpinning to the idea that flares (of all sizes) arise as avalanches of small scale reconnection events in complexly tangled coronal magnetic structures driven to criticality by photospheric forcing of their magnetic footpoints.

To the best of our knowledge, all attempts to date at comparing flare observations to SOC avalanche models have focused on the frequency distribution of quantities characterizing the temporal evolution of flare energy release, such as integrated and peak energy release, flare duration, and interflare waiting time (see [16]). This paper aims at establishing the basis for comparing the geometrical properties of avalanches in the SOC model, and flare observations at high spatial and temporal resolution. We first describe (Sec. II) the procedure whereby total thermal energy release in a flare is extracted from spatially resolved uv-euv observations, to highlight the importance of the assumed geometrical relationship between the observed flux-emitting projected area and the actual volume of flaring plasma. We then introduce and briefly discuss (Sec. III) a simple and well-studied SOC avalanche model for solar flares, and define various geometrical measures used in the discussion that follows. In Secs. IV and V we extract these geometrical measures from a variety of lattice simulations, in the course of which we establish the area/volume fractal relationship characterizing the avalanching regions in terms of the raw simulation results, their time-integrated equivalent, and/or projected versions thereof. We then (Sec. VI) examine the consequence of the fractal nature of the avalanching volume on estimates of the power-law index α_E of the flare energy frequency distribution. We conclude (Sec. VII) by reconsidering some of the issues raised above in the light of our modeling results.

II. CONVERTING uv-euv FLUXES INTO ENERGIES

The central issue in the analysis of flare data in the context of coronal heating is the conversion of uv-euv fluxes observed in a finite wavelength range, as in Fig. 1, to the total thermal energy $\mathcal{E}$ (in erg, say) released in the corona over the duration of the flare. Unfortunately, this thermal energy cannot be directly measured and must, therefore, be inferred from the observations. The inference of thermal energies from observed uv-euv fluxes is a complex procedure involving a number of assumptions regarding the physical conditions within the emitting volume, as well as its geometric properties. In the following we outline the recipe customarily followed to infer the total thermal energies of uv-euv flare events in order to give the reader an appreciation for the difficulties and assumptions involved.

The total spectral power P radiated above preflare quiescent background by an optically thin plasma of volume $\mathcal{V}$, in the uv-euv wavelength range of line or bandpass i, can be expressed as

$$P_i = \int_{\mathcal{V}} h\nu_i A_i n_{u(i)} d\mathcal{V} \text{ erg s}^{-1}, \tag{3}$$

where h is Planck's constant, ν_i is the frequency of the line, $A_i(\text{s}^{-1})$ is the Einstein A coefficient, and $n_{u(i)}$ (cm^{-3}) is the population density of the upper level of the atomic transition $u(i)$. The first step is to replace the volume integral by a double integral over electron density n_e and temperature T_e [17–19]. In doing so, a common working assumption, dubious physically but which we nonetheless adopt here since it is also made in most extant observational analyses, is to neglect the electron density dependence. The quantity that is actually observed, the spectral intensity $I_i = P_i/(4\pi\mathcal{A})$ for projected emitting area $\mathcal{A}$, is then given as

$$I_i = \int_{T_e} K_i(T_e)\xi(T_e) dT_e \quad \text{erg cm}^{-2}\ \text{sr}^{-1}\ \text{s}^{-1}, \tag{4}$$

where $\xi(T_e)$ is the differential emission measure in temperature (DEM [20,21]) and $K_i(T_e)$ is the line or bandpass emissivity.[2] The emissivity is a complex object (and even more complex for a wide wavelength bandpass, summed over the many constituent lines of the bandpass) that can be expressed in component form as

$$K_i(T_e) = \frac{h\nu_i A_i}{4\pi} \frac{n_{u(i)}}{n_{ion} n_e} \frac{n_{ion}}{n_{el}} \frac{n_{el}}{n_{\text{H}}} \frac{n_{\text{H}}}{n_e} \times \text{erg cm}^3\ \text{sr}^{-1}\ \text{s}^{-1}, \tag{5}$$

where $n_{u(i)}/n_{ion}$, n_{ion}/n_{el}, n_{el}/n_{H}, and n_{H}/n_e are the relative population of the upper atomic level of the line, the ionic abundance, elemental abundance, and relative abundance of H to electrons (having a value of 0.8 for the regions of the solar atmosphere considered in this paper), respectively.

The various terms on the right-hand side (RHS) of Eq. (5) determine the functional form of $K_i(T_e)$, which usually ends up being strongly peaked, and approximately Gaussian in shape due to the assumed Maxwellian electron distribution and the collisional contribution from the ionic abundance n_{ion}/n_{el}. The intensity can, therefore, be assumed to be proportional to the value of $\xi_i(T_e)$ in a narrow band (± 0.1 dex) (here dex stands for the base 10 logarithm of the temperature) about the peak temperature of line formation T_e^*. For the purposes of the present discussion we will, for simplicity, consider only emission at the peak temperature of the line emissivity, such that $K_i(T_e) = \mathcal{K}_i \delta(T_e - T_e^*)$, where $\delta(x - x_0)$ is the Dirac delta function and $\mathcal{K}_i$ is the peak magnitude at T_e^*. Now the integral of Eq. (4) becomes, converting to the integrated intensity flux f_i $(= I_i/\mathcal{A})$,

$$f_i \approx \frac{\mathcal{K}_i \xi(T_e^*)}{\mathcal{A}} \quad \text{erg cm}^{-4}\ \text{s}^{-1}, \tag{6}$$

where $\xi(T_e^*)$ is the value of the DEM at T_e^*. Assuming the form of $\xi(T_e) = n_e^2 dh/dT_e$ of Brown *et al.* [22] for scale height h, Eq. (6) makes it possible to derive an estimate of the electron density[3] in terms of the observed flux f_i. This requires an additional assumption, namely the form of the relation between the plasma scale height and the column

[2]The assumption of temperature dependence only is a gross simplification of the real situation since both the line emissivities and the DEM also depend on the electron density n_e of the emitting plasma.

[3]This assumes that the atmosphere is plane parallel in form, likely a reasonable approximation.

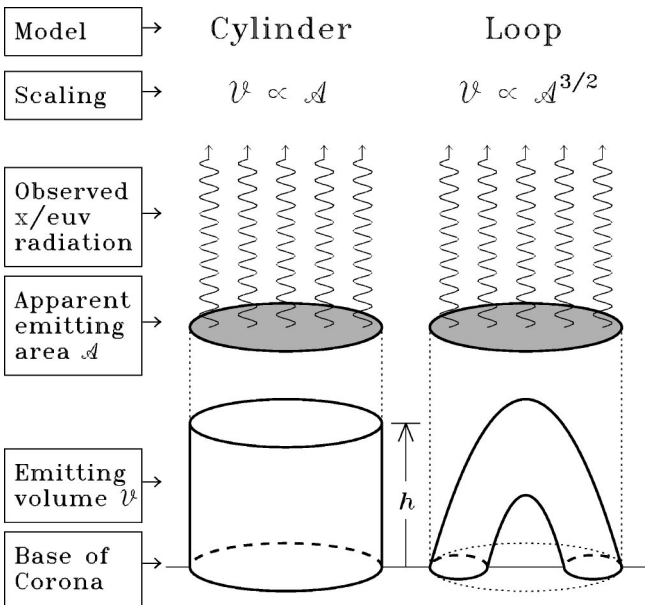

FIG. 2. Two simple and commonly used geometrical models relating the emitting area as seen in the observational plane ($\mathcal{A}$, in gray) to the actual volume ($\mathcal{V}$) of the emitting plasma. The observer is looking at the structures from above. In the cylinder model (left), $\mathcal{V}$ ends up directly proportional to $\mathcal{A}$ under the assumption of constant column depth h down to the base of the corona. The loop model (right) is characterized by a markedly different scaling: $\mathcal{V} \propto \mathcal{A}^{3/2}$.

depth. In the regime of a plasma with filling factor (ratio of emitting volume to total volume) unity, we have $\xi(T_e^*) = n_e^2 h$, so that

$$n_e = \sqrt{\frac{\xi(T_e^*)}{h}} \quad \mathrm{cm}^{-3}. \tag{7}$$

This estimate of n_e for the event allows us to estimate, at last, the thermal energy content $\mathcal{E}$ of the flaring plasma:

$$\mathcal{E} = 3 n_e k_B T_e^* \mathcal{V} \quad \mathrm{erg}, \tag{8}$$

where k_B $(=10^{-15.86}$ erg $\mathrm{K}^{-1})$ is the Boltzmann constant and $\mathcal{V}$ is, again, the volume of the emitting plasma, the final unknown quantity on the RHS of Eq. (8).[4] A geometrical model for the flaring volume is now introduced, so that $\mathcal{V}$ can be expressed in terms of the observed projected area $\mathcal{A}$. Figure 2 sketches the two geometrical models commonly used in the recent literature [7,24–26]. They lead to markedly different geometric scalings between $\mathcal{A}$ and $\mathcal{V}$, in turn leading to significant differences in estimates of volumetric energy release, namely, the ratio $\mathcal{E}/\mathcal{V}$, even when inferred from the same uv–euv–x-ray observations [7]. One is then naturally led to inquire as to the form of the $\mathcal{A}$-$\mathcal{V}$ relationship characterizing the avalanche model for solar flares, which is one of the central questions addressed in this paper.

[4]The electron pressure $p_e \propto n_e T_e^*$ is commonly assumed to be constant in isolated coronal regions, and determined observationally to be approximately at 4×10^{14} cm^{-3} K [23]. This then means that the thermal energy essentially scales as $\mathcal{E} \approx 3C\mathcal{V}$ ($C = 0.055$ erg cm^{-3}). Note also that Eq. (8) neglects any thermal energy content of the preflaring state, as well as other energy loss mechanisms that do not produce a radiative signature, such as thermal conduction, induced bulk flows, hydrogen ionization, generation of magnetohydrodynamic waves, to name but a few. These are all significant modeling assumptions.

III. AN AVALANCHE MODEL FOR SOLAR FLARES

We use a basic avalanche model for solar flares throughout. This model was primarily developed a decade ago by Lu and Hamilton [16,27,28] and is closely related to the classical sandpile model [13,14,29]. A (real-valued) field quantity B is defined on the nodes of a D-dimensional regular Cartesian lattice of linear size N; this field is subject to a self-stabilizing local threshold instability that leads to isotropic transport of B to neighboring lattice nodes whenever the stability threshold is exceeded; and the system is driven by adding small field increments at randomly selected lattice nodes, a process taking place only if all nodes are stable (the so-called ''slow driving'' limit). This avalanche model differs from the classical sandpile model primarily through its stability condition. The latter declares node k unstable whenever the magnitude of the nodal field B_k exceeds a preset threshold value Z_c:

$$B_k > Z_c \text{(height-triggered instability.} \tag{9}$$

In contrast, stability is lost in the present model whenever the local *curvature* of the field exceeds a preset threshold value:

$$\Delta Z_k \equiv \left| B_k - \frac{1}{2D} \sum_{\mathrm{NN}} B_{\mathrm{NN}} \right| > Z_c$$

$$\text{(curvature-triggered instability)}, \tag{10}$$

where the index NN stands for the 2D nearest neighbors on the Cartesian lattice, and D is the lattice dimension ($D=3$ is usually adopted in the flare modeling context). Whenever a node is deemed unstable, B_k is redistributed to neighboring nodes in a manner such that stability is restored at that node. For a given set of such rules, models based on either of Eqs. (9) or (10) behave in a qualitatively similar manner in that they are naturally driven to a self-organized critical state, in which the dissipation of B occurs intermittently via avalanches of redistribution events. The redistribution rules used to restore local stability in the curvature-triggered model are conservative in B, but lead to a decrease in B^2 summed over the nodes involved in the redistribution. With B associated with a magnetic field, B^2 becomes a measure of magnetic energy, thus implying that energy is ''dissipated'' locally at each avalanching node, in amounts (e_k) that, in general, vary from node to node:

$$e_k = \frac{6}{7}\left(2\frac{\Delta Z_k}{Z_c} - 1 \right) Z_c^2. \tag{11}$$

The net energy dissipated over the whole lattice at the current model iteration (t) is thus simply $E_t = \Sigma e_k$, where the sum extends over all unstable nodes. Let now t_0 denote the (timelike) iteration number at which an avalanche begins, and T its duration, also measured in timelike iteration units. The total energy dissipated in the course of the avalanche is then simply

$$E = \sum_{t_0}^{t_0+T} E_t, \tag{12}$$

while the peak energy dissipation rate (P) is

$$P = \max(E_t), \quad t \in [t_0, t_0+T]. \tag{13}$$

The frequency distributions of these avalanche parameters have the form of declining power laws with logarithmic (base 10) slopes[5] of order unity. However, the detailed examination of the frequency distributions reveals that the height- and curvature-triggered models belong to different universality classes [30]. In addition, the vector-scalar character of B has been shown to have no influence on the statistical behavior of the model, at least for regular lattices, redistribution rules, and driving mechanisms usually considered [31]. Hence, we will proceed with the computationally less intensive scalar version of the model, even though the use of a vector field turns out to be physically preferable. For a complete description of the model, and review of variations thereof, see [16]. In the solar flare context, the reasonably good agreement between the frequency distributions for P and E in the curvature-triggered model and their observational counterparts reconstructed from time series of solar uv–euv–x-ray emission [27,28] have provided much of the impetus for further elaborations of SOC avalanche models for solar flares.

On the other hand, the geometrical properties of avalanches in such models remain largely unexplored. Among the many possible ways of approaching this issue, the determination of fractal dimensions represents an obvious avenue. We extract these from the model output in the following fashion. Figure 3(a) shows a snapshot of an avalanche at the peak of its energy release, extracted from a simulation on a two-dimensional lattice of size 128×128. Avalanching nodes are shown in white. Let $\mathbf{r}_i$ be the position of the ith avalanching node, measured from some arbitrary but fixed reference point in the lattice. The center of mass ($\mathbf{R}_0$) and radius of gyration (R) of the cluster of avalanching nodes are given by

$$\mathbf{R}_0 = \frac{1}{V} \sum_{i=1}^{V} \mathbf{r}_i, \tag{14}$$

$$R^2 = \frac{1}{V} \sum_{i=1}^{V} |\mathbf{r}_i - \mathbf{R}_0|^2, \tag{15}$$

[5]For brevity, hereafter, we will use logarithm, or log, to express a base 10 logarithm. Indeed, base 10 logarithms are used exclusively in this paper.

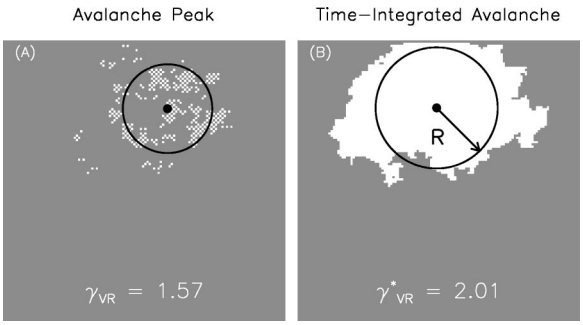

FIG. 3. The spatial structure of an avalanche in a two-dimensional 128×128 lattice. (a) shows the avalanche at its peak when some 329 nodes are unstable and (b) shows the time-integrated avalanche, where some 4179 nodes have gone unstable at least once over the course of the avalanche. Also shown are the avalanche centers of mass (solid dot), and the circle mapped by the radius of gyration for both situations. The fractal indices at the avalanche peak γ_{VR} and of the time-integrated avalanche γ^*_{VR} are 1.57 and 2.01, respectively. The time-integrated avalanche cluster in (b) is a compact object, whereas that of (a), at the peak, is not.

where V is the volume of the avalanche cluster, defined simply as the number of avalanching nodes[6]. The radius of gyration is a common measure of linear cluster size used in percolation theory [32] and corresponds to the radius of the thin annulus in two dimensions (spherical shell in three dimensions) having the same ''mass'' and moment of inertia as the original cluster. The fractal dimension (γ_{VR}) of the cluster is then straightforwardly defined through the relation

$$\log_{10}(V/V_0) = \gamma_{VR} \log_{10} R, \tag{16}$$

and is the logarithmic slope, obtained via linear least-squares fit, of the (log-log) scatter plot of volume V versus R for all avalanches recorded in the course of a given simulation.

Another quantity that is accessible observationally is the logarithmic slope of the power-law frequency distributions of avalanche parameters. As already introduced in Eq. (1), this slope will be denoted by the letter α, subscripted by the corresponding avalanche parameter (V, R, etc.):

$$\log_{10}[f(V)/f_0] = -\alpha_V \log_{10} V. \tag{17}$$

Such power laws are found to hold up to an upper cutoff which itself scales with the lattice size, indicative of finite-size scaling [29,28].

In the context of flare observation a practical difficulty immediately arises. The integration time of current solar uv-euv imaging instruments is often comparable to the characteristic internal time scale for flare evolution. Figure 3(a) is

[6]Strictly speaking, the physical volume (in cm^3) is the number of avalanching nodes times the (unit) volume of a lattice cell. All geometric quantities assessed in the models (V, R, etc.) are measured in dimensionless units scaled to the internodal distance in the lattice. Note also that we use ''volume'' even in the $D=2$ case, where ''area'' would be geometrically preferable but notationally confusing in what is soon to follow in Sec. V.

TABLE I. A compilation of symbols used in this paper to characterize the spatial and temporal properties of avalanches, and associated power-law indices.

Symbol	Definition
E	Time-integrated energy release
P	Peak energy release
T	Duration of avalanche
V	Avalanche volume ($\equiv$ number of avalanching nodes)
R	Radius of gyration of avalanching cluster
γ_{yx}	Logarithmic slope of y vs x correlation plot
α_x	Logarithmic slope of frequency distribution for x
A	Projected area of avalanching cluster
Γ_{yx}	Similar to γ_{yx}, but for projected quantities

thus a very idealized view of a flare. At the other extreme one can imagine a situation where the integration time is comparable to the duration of the flare or avalanche. Figure 3(b) shows the cluster of all nodes having gone unstable at least once in the course of the avalanche. One can again define a radius of gyration and compute a fractal dimension for this geometrical object, via Eq. (16), but there is no *a priori* reason to expect that the fractal dimension so computed will be identical to that obtained from the instantaneous snapshot of Fig. 3(a).

In the following sections, in order to assess the consequences of such time-integration effects, we examine the geometrical properties of avalanches in the two extreme cases shown in Fig. 3; namely, the ''highest'' and ''lowest'' temporal resolution. Specifically, we extract avalanche parameters from a single-iteration snapshot at their peak (highest resolution), and from time integration over the duration of the whole avalanche (lowest resolution). We use an asterisk to distinguish between the quantities associated with the latter situation, leaving quantities computed from avalanche peak snapshots without superscripts. For example, γ_{VR} denotes the power-law slope of the V vs R correlation plot for the avalanche peaks [Fig. 3(a)], while α_V^* denotes the power-law index of the size frequency distribution for time-integrated avalanche volumes [Fig. 3(b)]. For quick reference, Table I compiles a list of the various symbols used to describe avalanche parameters and associated power-law indices.

IV. GEOMETRICAL PROPERTIES OF AVALANCHES

Our first task is to compute fractal dimensions and logarithmic slopes of the frequency distributions for the various avalanche parameters. We do so for a variety of linear lattice sizes (N) and spatial dimensions (D, restricted to 2 or 3 here). Given the natural variability of the SOC state, we accumulate statistics for series of independent runs, in order to extract meaningful Monte Carlo–like error bars (for further discussion of this point, see [16], Sec. 2.9). Results are compiled in Table II. Power-law indices for the frequency distributions of peak energy release P and avalanche duration T are listed in Table 2 of [16], for the same curvature-triggered lattice model, and are not replicated here since they are not central to the present discussion.

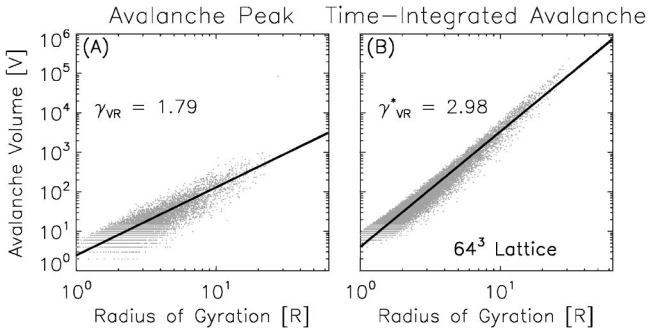

FIG. 4. A typical power-law relationship between the avalanche volume V and its radius of gyration R for simulations carried out on an $N^D=64^3$ lattice, in the course of which approximately 0.27×10^6 avalanches were recorded. In (a) we show the distribution of values at the peak of the avalanche, and those of the time-integrated avalanche in (b). Both scatter plots are well-fitted, by a power-law relationship. The least-squares best-fit lines in both cases give logarithmic slope values $\gamma_{VR}=1.79$ and $\gamma^*_{VR}=2.98$ for panels (a) and (b), respectively.

In general, the correlations between pairs of avalanche parameters are rather tight, so that the logarithmic slopes are determined with good accuracy. Figure 4 shows two representative correlation plots of V vs R for the peak instantaneous (left) and time-integrated (right) distributions of avalanching nodes, from which the corresponding fractal dimensions γ_{VR} and γ^*_{VR} are obtained. The resolution of the lattice leads to increased scatter at small values of avalanche parameters, and its finite size imposes an upper cutoff on R, which translates into the slight upturn visible for the largest avalanches. Nonetheless, Table II shows that the inferred power-law indices remain stable as lattice size is varied.

Examining the third column of Table II also shows that time-integrated avalanches have $\gamma^*_{VR}=D$ to within the error bars, i.e., the time-integrated avalanche is a geometrically compact object. On the other hand, avalanches at their peak have $\gamma_{VR}<D$, and so are fractal objects in the usual sense. Not surprisingly, this geometrical distinction carries through to the frequency distributions of avalanche volumes (cf. the fourth and fifth columns of Table II).

As might be expected from the self-similar nature of avalanches, the geometric parameters V and R have frequency distributions described by well-defined power laws, whether one considers the peak or time-integrated distribution of avalanching nodes. Remarkably, there is no statistically significant difference between the α_V indices obtained in two and three spatial dimensions, unlike those of other avalanches parameters such as duration and total energy release (cf. Table 2 of [16]). We could not construct a simple, intuitively obvious explanation as to why it is so, but this is evidently a robust property of the model, judging from the stability of the α_V indices with respect to variations in the lattice size.

Comparing the sixth and seventh columns of Table II also reveals that $\gamma_{PV}\simeq\gamma^*_{EV}$ within the error bars. This indicates that, on average, each avalanching node releases roughly the same amount of energy once the avalanche gets underway, even though nodal energy release is not constant in the

TABLE II. Power-law indices for correlation plots (γ) and size frequency distribution (α) for series of lattice simulation carried out for either two or three spatial dimensions (D), and a variety of linear lattice sizes (N). These quantities are computed at avalanche peak and for the time-integrated avalanches, the latter identified by an asterisk. In particular, we show the avalanche fractal dimensions (γ_{VR}, γ^*_{VR}), the power-law exponents of the avalanche total energy and volume frequency distributions (α_E, α_V, α^*_V), and the model volumetric energy release (γ_{PA}, γ^*_{EA}).

N^D	γ_{VR}	γ^*_{VR}	α_E	α_V	α^*_V	γ_{PV}	γ^*_{EV}
32^2	1.61 ± 0.02	2.01 ± 0.04	1.42 ± 0.00	1.03 ± 0.06	0.55 ± 0.05	1.06 ± 0.07	1.09 ± 0.08
64^2	1.60 ± 0.02	2.02 ± 0.05	1.41 ± 0.00	1.05 ± 0.07	0.52 ± 0.03	1.04 ± 0.04	1.07 ± 0.05
128^2	1.57 ± 0.03	2.01 ± 0.06	1.40 ± 0.00	1.02 ± 0.06	0.55 ± 0.02	1.02 ± 0.03	1.06 ± 0.04
256^2	1.55 ± 0.02	2.00 ± 0.04	1.41 ± 0.00	1.01 ± 0.08	0.51 ± 0.04	1.07 ± 0.05	1.05 ± 0.05
512^2	1.56 ± 0.04	2.00 ± 0.05	1.42 ± 0.01	1.04 ± 0.04	0.52 ± 0.04	1.05 ± 0.03	1.04 ± 0.03
16^3	1.78 ± 0.03	3.05 ± 0.04	1.45 ± 0.00	1.03 ± 0.05	0.49 ± 0.03	1.02 ± 0.08	1.12 ± 0.09
24^3	1.77 ± 0.04	3.00 ± 0.02	1.46 ± 0.00	1.04 ± 0.03	0.48 ± 0.04	1.01 ± 0.05	1.09 ± 0.06
32^3	1.80 ± 0.03	2.98 ± 0.02	1.46 ± 0.00	1.05 ± 0.04	0.50 ± 0.04	1.00 ± 0.03	1.08 ± 0.06
48^3	1.78 ± 0.03	2.98 ± 0.03	1.47 ± 0.01	1.04 ± 0.04	0.51 ± 0.05	1.00 ± 0.01	1.09 ± 0.05
64^3	1.79 ± 0.02	2.98 ± 0.03	1.47 ± 0.00	1.02 ± 0.04	0.49 ± 0.04	1.00 ± 0.01	1.08 ± 0.05

present curvature-triggered model. The marginally larger values of γ^*_{EV} reflect the fact that our definition of V for the time-integrated avalanche is such that nodes avalanching more than once only contribute one ''unit'' to V, while contributing more toward the total energy E than a node having avalanched only once. Hence the E vs V correlation is steeper.

V. PROJECTION EFFECTS

In seeking to compare model results to observations, one must recognize that what is observed is a *projection* of the flaring volume onto the plane of the sky. Figure 5 illustrates the situation. The left diagram is a three-dimensional equivalent of Fig. 3(b), namely, the three-dimensional cluster comprised of each node having gone unstable at least once in the course of the avalanche (note already how this bears little resemblance to either the cylinder or loop model of Fig. 2). The three panels on the right show the shape of this cluster, projected on the three coordinate planes, where the gray scale encodes the number of avalanching nodes along the line of sight. This amounts to saying that all energy released by avalanching nodes located along the line of sight is visible along that line of sight. We will refer to this as the ''optically thin'' assumption.[7]

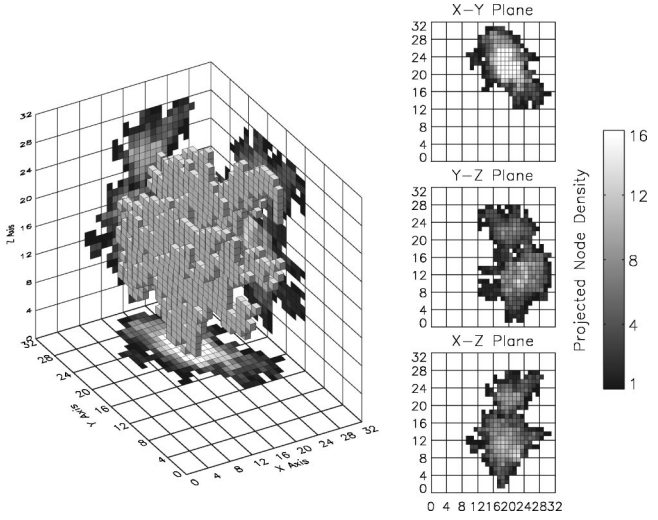

FIG. 5. The three-dimensional structure of the time-integrated avalanche in an $N^D=32^3$ lattice. Here 5145 nodes have gone unstable at least once over the duration of the avalanche. The right hand side of the figure shows direct views of the projections of the time-integrated cluster on the three coordinate planes of the lattice. The gray scale in the projected planes indicates the number of avalanching nodes, or column depth, along the projection line of sight.

It should be clear from Fig. 5 that the geometrical properties of the actual flaring volume cannot be retrieved unambiguously from the geometrical properties of the projected areas (and even less so if only one projection is available, which is the case when analyzing current observational data). Consequently, we now examine the geometrical properties of the three projections onto the orthogonal two-dimensional lattice planes, as on Fig. 5, which is computationally most convenient and entails no loss of generality. The analysis follows that carried out in the preceding section, except that we now introduce the projected avalanche area A, defined as the cluster of nodes in the two-dimensional planes for which at least one node along the corresponding perpendicular line of sight is avalanching. As before we consider the avalanches at their peak and as time-integrated objects. Because of the optically thin assumption, the total and peak energy release E and P, as well as the avalanche duration T, are unaffected by the projection, so that the corresponding frequency distributions are also unchanged. On the other hand, the distribution of projected areas A and corresponding radii of gyration are now distinct from the truly three-dimensional situation. To distinguish between these related situations we use an upper-

[7]This is also the assumption made when carrying out analyses of the Sun's uv–euv–x-ray emission.

TABLE III. Equivalent power-law indices to those listed in Table II, but now computed from the projection of three-dimensional avalanches onto the three orthogonal coordinate planes of the lattice. The logarithmic slopes of correlation plots involving projected avalanches are denoted using Γ, reserving γ for unprojected quantities.

N^D	Γ_{AR}	Γ^*_{AR}	α_A	α^*_A	Γ_{PA}	Γ^*_{EA}
16^3	1.48 ± 0.09	1.96 ± 0.05	1.19 ± 0.05	0.59 ± 0.02	1.12 ± 0.05	1.64 ± 0.12
24^3	1.52 ± 0.07	1.97 ± 0.04	1.17 ± 0.04	0.60 ± 0.04	1.09 ± 0.03	1.62 ± 0.08
32^3	1.52 ± 0.06	1.97 ± 0.05	1.15 ± 0.04	0.62 ± 0.03	1.08 ± 0.02	1.60 ± 0.05
48^3	1.49 ± 0.05	1.98 ± 0.07	1.20 ± 0.04	0.63 ± 0.03	1.07 ± 0.03	1.59 ± 0.04
64^3	1.53 ± 0.06	1.96 ± 0.06	1.12 ± 0.05	0.63 ± 0.03	1.07 ± 0.03	1.59 ± 0.04

case gamma (Γ) to denote logarithmic slopes—including fractal dimensions—associated with avalanches seen in projection.

The results are compiled in Table III and pictorially buttressed by Fig. 6, which demonstrate—among other things—that once again the geometric parameters are related via well-defined power laws. In addition, the inferred power-law indices exhibit robustness with respect to grid size, with variations well within the Monte Carlo error bars, except in some cases for the smallest lattice considered ($N=16$). The projected time-integrated avalanches are again compact objects ($\Gamma^*_{AR}=2$), which of course was to be expected since the underlying time-integrated three-dimensional avalanche is itself a compact object ($\gamma^*_{VR}=3$). Note also that for the avalanche peak $\Gamma_{AR}(D=3)\simeq\gamma_{VR}(D=2)$, indicating that the projected three-dimensional avalanches are geometrically similar to $D=2$ avalanches.

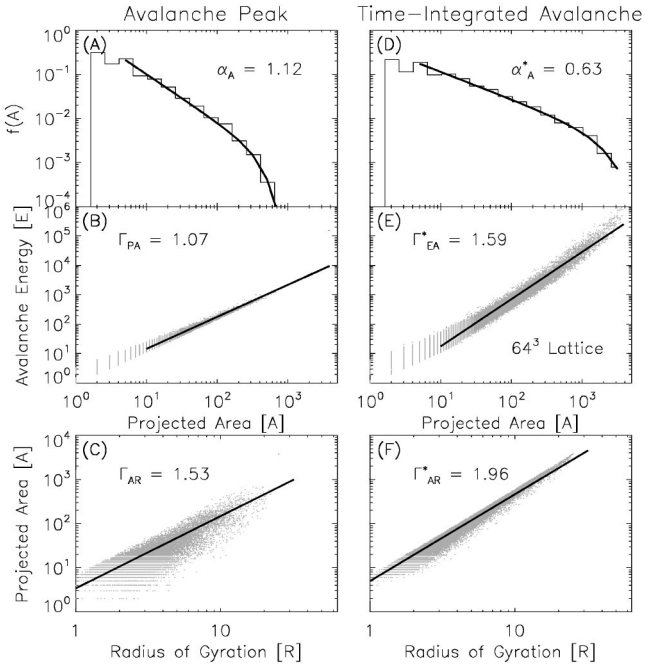

FIG. 6. A sample of various power-law relationships and frequency distributions formed by combinations of the geometrical properties of three-dimensional avalanches projected onto the two-dimensional planes (cf. Fig. 5), constructed here from an $N^D=64^3$ lattice simulation. Results for avalanche peak snapshots are shown in (a)–(c) while those for time-integrated avalanches are shown in (d)–(f). Many differences are immediately clear between these two sets of plots: the frequency distribution of projected areas is much flatter in (d) than in (a); (e) demonstrates a large energy release per unit area, compared to that at avalanche peak (b); the different fractal dimensions of the avalanches as seen in projection [see, e.g., Figs. 5(c) and 5(f)].

In view of the optically thin assumption, a node of the projected area now "accumulates" the energy released along the whole corresponding line of sight. The superposition of nodes along the line of sight leads to an increase in the number of geometrically small avalanches and, therefore, gives rise to a steeper frequency distribution for A; likewise, the steepening of the P and E vs A power-law relationships due to the enhancement of the energy recorded per unit area. Further, we see that these cumulative effects are particularly pronounced for the time-integrated avalanches (compare α_A, α^*_A, Γ_{PA}, and Γ^*_{EA} in Table III to α_V, α^*_V, γ^*_{PV}, and γ^*_{EV} in Table II).

VI. COMPARISON WITH FLARE OBSERVATIONS

Before we launch in earnest into the comparison between model results and flare observations, it is important to clarify the assumptions under which such comparisons are to be made. There is no "plasma" in the avalanche models, only an idealized representation of a magnetic field–related quantity sampled on a finite lattice. We can imagine that this lattice, and the field defined on it, are embedded in a dynamically passive plasma, whose only purpose is to absorb and radiate away the energy dissipated within it by avalanches. If we then assume that all of the energy dissipated at avalanching nodes goes into localized heating of this plasma, then the energy dissipation computed via Eq. (12) becomes directly proportional to the thermal energy in Eq. (8), i.e., $\mathcal{E}\propto E$. If we further assume that the energy so dissipated heats the plasma within a volume comparable to the unit lattice cell size, then a cluster of unstable nodes (e.g., Fig. 5) become a measure of the emitting volume in Eq. (8), so that $\mathcal{V}\propto V$, and likewise for the projected areas $\mathcal{A}\propto A$. Turning these proportionality relations into equalities requires that physical units be introduced in the lattice model. This is certainly possible (see, e.g., [28]), but actually not required in the comparison of model and observed power-law scatter plots and frequency distributions, in view of their self-similar character.

There are only a few extant observational determinations

TABLE IV. The logarithmic slopes of the power-law relationships formed by the volume V and the *projected* area A subtended by the avalanches on three-dimensional lattices of various linear size. Once again values are listed for snapshots at the avalanche peak (γ_{VA}) and for the time-integrated avalanche (γ^*_{VA}).

N^D	γ_{VA}	γ^*_{VA}
16^3	1.11 ± 0.06	1.44 ± 0.05
24^3	1.09 ± 0.07	1.41 ± 0.04
32^3	1.08 ± 0.08	1.40 ± 0.03
48^3	1.07 ± 0.06	1.42 ± 0.04
64^3	1.07 ± 0.05	1.41 ± 0.04

of the size frequency distribution of projected flaring areas [7,33–35]. Those studies indicate that $f(A)$ is a declining power-law over a bit more than an order of magnitude in projected area A, at best. The inferred power-law indices cover a broad range, from $\alpha_A \simeq 1.3$ to 2.7. Our model results (Fig. 6) yield $\alpha_A = 1.12 \pm 0.05$, which is marginally compatible with [34], but the time-integrated index $\alpha^*_A = 0.63$ is much smaller than the presumably equivalent index inferred by [7]. Although a fairer comparison with this latter study would require replicating their ellipse fitting procedure to determine A (as opposed to counting projected model pixels, as done here), it appears that a real discrepancy between model and observations may exist at the level of the distribution of projected areas. How severe a discrepancy this is will likely be hard to estimate, because of the tricky issue of observational detection threshold in deciding whether a given pixel is part of a flare (see the discussion in [26]), but this is an issue that could, in principle, be explored using our model results. At any rate, the logarithmic slope of the area frequency distribution of flares certainly offers a powerful observational test of the avalanche model.

As discussed at the end of Sec. II, a quantity of particular interest in the context of observational analyses of solar uv–euv–x-ray emission is the relationship between the (two-dimensional) observed emitting area $\mathcal{A}$ and the underlying (three-dimensional) flaring volume $\mathcal{V}$ [cf. Eq. (8) and Figs. 1 and 2]. We can address this question using our model results by simply making the assumption that $\mathcal{V} \equiv V$ and $\mathcal{A} \equiv A$, as discussed earlier. Table IV lists the relevant power-law indices, once again, as inferred from a snapshot of avalanches at their peak (γ_{VA}), and integrated over the avalanche duration (γ^*_{VA}), with Fig. 7 showing representative correlation plots to demonstrate once again how well defined the power-law relationships actually are.

That γ^*_{VA} should be significantly larger than γ_{VA} is again a consequence of the fact that, in the time-integrated avalanche, far more nodes contribute to a ''unit'' of A than in the peak snapshot. Consequently, V increases more rapidly with A in the former case. The reader can best appreciate this situation by returning to Fig. 3 and noting how the two clusters plotted therein have comparable projected lengths along the horizontal and vertical axes, yet the cluster in Fig. 3(b) has a volume ($\equiv$ number of nodes) nearly 13 times greater.

It is indeed remarkable—and entirely unexpected—that the power-law indices characterizing the V vs A relationships

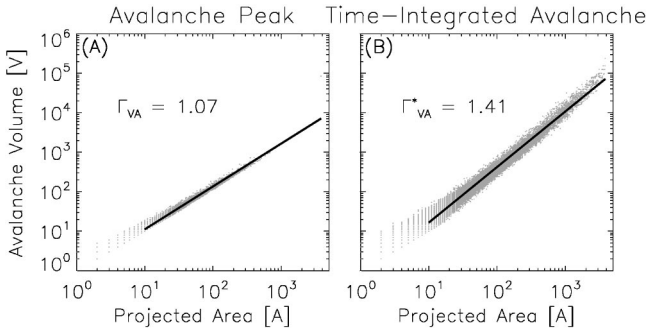

FIG. 7. Power-law relationships between the volume V and the projected area A of avalanching node clusters on an $N^D = 64^3$ lattice at peak (a) and integrated over time (b). Both scatter plots define statistically tight relationships, but the values of the corresponding logarithmic slopes Γ_{VA} and Γ^*_{VA} are markedly different. As in Fig. 6(e), the upturn visible in the upper right of (b) is due to the finite size of the lattice, which here limits the projected area to $(N-2)^2 = 3844$ (boundary nodes cannot avalanche in our lattice model).

for our two extreme cases (instantaneous snapshots and time-integrated avalanche) are bracketed by those associated with the two simple geometrical models introduced in Fig. 2 (1.0 and 1.5, respectively). Both are defined in terms of geometrically compact objects, namely, a cylinder and an arched cylindrical loop, yet even the compact, time-integrated avalanches yield a different V-A scaling.

The analysis carried out in [7] of 281 euv nanoflares observed by TRACE leads to a power-law relationship between the released thermal energy $\mathcal{E}$ and the observed projected area $\mathcal{A}$ with index equal to $\Gamma^*_{EA} = 1.44$ (in our notation; see [7], Fig. 5). This is quite close to the corresponding value listed in in Table III here, namely, $\Gamma^*_{EA} = 1.59 \pm 0.04$ (for our largest lattice, $N^D = 64^3$). This good agreement should not be overinterpreted, however, at it is for the most part a secondary consequence of the (remarkable) similarity between the area-volume relationship characterizing the two models: $\gamma^*_{VA} = 1.44$ for the loop model[8] versus $\gamma^*_{VA} = 1.41$ for the avalanche model.

What then are the consequences of such geometrical effects for Parker's conjecture of coronal heating by nanoflares? As already mentioned in Sec. I, the answer hinges on the logarithmic slope of the frequency distribution of energy release (α_E in our notation), in which the V-A relationship of the flaring volume is but one of the determining factors. It is possible to use the results presented here to compute (in a preliminary manner and with all due caution) a ''correction'' to previously published observational analyses using different geometrical models.

The crux of the matter is to express the observationally inferred frequency distribution $f(E)dE$ in terms of a new energy release variable $E' [= s(E)E]$ corrected for geometri-

[8]The loop model used in [7] incorporates an observationally determined area filling factor, which is found to scale with the area itself; this is why the power-law index of the inferred $\mathcal{V}$-$\mathcal{A}$ relationship deviates from the value 1.5 associated with the basic loop model of Fig. 2, which assumes a constant filling factor.

TABLE V. Geometrical ''corrections'' to three recent analyses of uv-euv flare energy release.

Reference	Geometrical model	β	α_E	$\alpha_E+\Delta\alpha$
[25]	Cylinder, constant h	1.0	2.3–2.6	1.77–1.94
[24]	Cylinder, constant h	1.0	2.42	1.84
[7]	Loop [a]	1.44	1.79 ± 0.08	1.81 ± 0.09

[a]See footnote 7.

cal rescaling in terms of the fractal dimension of avalanches. The three observational analyses considered below [25,24,7] work with what corresponds, in the language of the present paper, to time-integrated avalanches. Let β be the logarithmic slope of the *V*-*A* relationship for either one of the geometrical models of Fig. 2, and $\gamma\equiv\gamma^*_{VA}$ henceforth, to lighten the notation. The correction factor s to the inferred emitting volume is then

$$s(A)=A^{\gamma-\beta}. \tag{18}$$

Under the (common) assumption of constant pressure [$\propto n_eT_e$ in Eq. (8)], the only remaining dependence of $\mathcal{E}$ is on the emitting volume $\mathcal{V}$. Again, under the ansatz $\mathcal{E}\equiv E$, $\mathcal{V}\equiv V$, and $\mathcal{A}\equiv A$, this then implies $A\propto E^{1/\beta}$, and thus

$$s(E)=E^{(\gamma-\beta)/\beta}. \tag{19}$$

We now need to express $f(E')dE'$ in terms of $f(E)dE$. With the latter given by the power law $f(E)=f_0E^{-\alpha_E}$, some straightforward algebra soon leads to

$$f(E')dE'=f(sE)\frac{dE'}{dE}dE\propto f(E)dEE^{\Delta\alpha}$$
$$=f_0E^{-(\alpha+\Delta\alpha)}dE, \tag{20}$$

where the correction factor $\Delta\alpha$ to the power-law index α_E is given by

$$\Delta\alpha=\frac{(1-\alpha_E)(\beta-\gamma)}{\beta}. \tag{21}$$

Table V lists the α_E values inferred from these three recent observational analyses of uv-euv data, together with the ''corrected'' values obtained by adding $\Delta\alpha$, as computed above. It is quite remarkable that this simple-minded correction for purely geometrical effects brings all three inferences into much better agreement than in their original form.

VII. SUMMARY AND DISCUSSION

We have examined in some detail the geometric properties of avalanches in an established SOC model for solar flares [15,16,27,28]. The fractal structure of avalanches, coupled with projection effects, is found to yield a distinctly different volume/projected area relationship than nonfractal geometrical models routinely used in the analysis of flare data. This leads to a different observationally inferred power-law index α_E for the frequency distribution of energy release, and thus to potentially distinct conclusions regarding the contribution of nanoflares to solar coronal heating.

While the focus of this paper has been on the geometric properties of avalanches, other factors also significantly influence the determination of the frequency distribution of energy release by small flares observed in uv–euv–x-ray regions. It has now been amply demonstrated (see, e.g., [7]) that the selection criteria adopted to select ''flares'' from other brightness variations also have a marked influence on the inferred value of α_E. In addition, as outlined in Sec. VI here, the vast majority of observational analyses published to date make a number of simplifying assumptions in relating the observed fluxes to volumetric energy release, notably the lack of dependence of the DEM on the electron density, and the assumed pressure distribution in the flaring volume. These are also issues of critical importance in assessing whether or not nanoflares can be held responsible for coronal heating. Indeed, by introducing additional *ad hoc* (but plausible) dependencies on E, for example, on the column depth and/or the DEM itself, it is certainly possible to produce a wide range of logarithmic slopes for the model $f(E)$ [36].

The (simplistic) attempt made in Sec. VI to correct for the fractal geometry of avalanches in the SOC flare model has led to the interesting result that widely varying estimates of α_E inferred by recent observational analyses have been brought into closer agreement. This should serve to reemphasize that geometrical assumptions play a critical role in the determination of the frequency distribution of energy release events from solar observations. On the other hand, this should not blind us to the fact that a significant discrepancy still remains, namely, the fact that the value of α_E extracted directly from the avalanche model ($\alpha_E\simeq1.5$, cf. Table II here) remains significantly lower than even the ''corrected'' observationally inferred values listed in Table V. One possible solution to this dilemma invokes the unavoidable temperature bias associated with narrowband observations. A recent Monte Carlo simulation [37] aimed at correcting for this observational bias indicates that this can bring the observationally inferred α_E into much better agreement with the prediction of the avalanche model. Alternately, various mechanisms have been proposed to steepen the $f(E)$ distribution produced by the flare avalanche model (see [16], Secs. 3.2, and 3.3, and references therein). However, the fractal dimensions of avalanches in these modified models remain to be determined.

Nonetheless, the high spatial resolution and temporal cadence observations provided by the latest generation of solar observing space-borne instruments such as those on SOHO and TRACE allow us to ''see'' avalanches in progress. This offers a hitherto unexplored point of comparison between observations and SOC models. This paper has barely scratched the surface of this comparison, but has already identified a potential discrepancy between model and observations, namely, that the former predict much flatter power-law frequency distributions of projected areas than those inferred observationally. How severe this discrepancy actually is is hard to estimate, given the wide range of observational α_A's. Two aspects relevant to this problem, which we plan to pursue in due course, are the issues of the spatial fragmen-

tation of avalanches and the effects of noise and detection thresholds, both of which have important consequences for observational analyses.

The avalanche model of solar flares provides an attractive and thus far quite successful framework within which to interpret observed flare statistics. However, at first glance such models have little to say about the microphysics of the reconnection process itself, since the statistical behavior of the model does not depend sensitively on the numerical detail of the stability and redistribution rule formulation (provided certain general constraints are satisfied, such as the presence of a finite instability threshold, and locality and isotropy in the redistribution, for example). However, interesting aspects of the relevant microphysics can still be recovered. It is possible to ''reverse-engineer'' a continuum partial differential equation (PDE) from the discrete stability and redistribution rules, and to relate this PDE to the magnetohydrodynamic (MHD) equations [16,38,39]. In particular, recent work [39] along these lines indicates that the field transport occurs via a diffusivelike process mathematically akin to MHD turbulence, suggesting in turn that, under solar coronal conditions, magnetic reconnection at single flaring sites becomes turbulent shortly after onset.

In closing, it is worth reiterating that, unlike many other applications of sandpile models to complex physical systems, here Parker's picture of a photospherically anchored and driven, complexly tangled coronal magnetic fields provides a sound physical underpinning to the SOC picture [10,15,16,38,40]. With the field quantity B identified with a measure of the magnetic vector potential ($\mathbf{A}$, such that the magnetic field $\mathbf{B}=\nabla\times\mathbf{A}$), the instability sets in once the local electric current ($\propto\nabla^2\mathbf{A}$ for a suitable choice of electrostatic gauge) exceeds a threshold value, which fits nicely with current ideas about magnetic reconnection under solar coronal conditions; local redistribution of A does lead to reduction of the local electric currents and associated energy release; addition of small $\mathbf{A}$ increments amounts to localized increases in the twist of the magnetic field; the separation of time scale between driving and avalanching is also well justified in the coronal context, with photospheric fluid motions (driving) operating on time scales of hours to days, while internal field readjustment and reconnection (avalanching) take place in seconds to minutes under typical solar coronal conditions. Indeed, energy release in solar flares represents a very convincing physical example of SOC, well on a par with seismic energy release in earthquakes. Moreover, avalanche models based on Parker's nanoflare picture can, in principle, address the physical nature of both flares and coronal heating within the same unifying framework, a truly remarkable state of affairs if vindicated.

ACKNOWLEDGMENTS

This paper is a by-product of the activities of the SOC working group at HAO/NCAR. S.W.M. is currently supported by the ESA at NASA/GSFC, and was formerly supported at NCAR (HAO and ASP divisions) where this work was initiated. H.L.L. is partly supported through NASA Grant No. S-97239-E to NCAR. J.P.N. acknowledges the hospitality at HAO during a visit. We also wish to to thank Dawn Myers for her assistance in handling the TRACE data presented. The National Center for Atmospheric Research is sponsored by the National Science Foundation.

[1] E. R. Priest and T. G. Forbes, *Magnetic Reconnection: MHD Theory and Applications* (Cambridge University Press, Cambridge, England, 2000).
[2] G. L. Withbroe and R. W. Noyes, Annu. Rev. Astron. Astrophys. **15**, 363 (1977).
[3] B. Dennis, Sol. Phys. **100**, 465 (1985).
[4] *The SOHO Mission*, edited by B. Fleck, V. Domingo, and A. I. Poland (Kluwer, Dordrecht, 1995).
[5] J.-P. Delaboudinière *et al.*, in *The SOHO Mission* (Ref. [4]).
[6] B. N. Handy *et al.*, Sol. Phys. **187**, 229 (1999).
[7] M. J. Aschwanden *et al.*, Astrophys. J. **535**, 1047 (2000).
[8] H. S. Hudson, Sol. Phys. **133**, 357 (1991).
[9] E. N. Parker, Astrophys. J. **264**, 642 (1983).
[10] E. N. Parker, Astrophys. J. **330**, 474 (1988).
[11] E. N. Parker, *Spontaneous Current Sheets in Magnetic Fields* (Oxford University Press, New York, 1994).
[12] P. Bak, *How Nature Works* (Springer, New York, 1996).
[13] P. Bak, C. Tang, and K. Wiesenfeld, Phys. Rev. Lett. **59**, 381 (1987).
[14] H. J. Jensen, *Self-Organized Criticality* (Cambridge University Press, Cambridge, England, 1998).
[15] E. T. Lu, Astrophys. J. Lett. **446**, L109 (1995).
[16] P. Charbonneau, S. W. McIntosh, H. Liu, and T. J. Bogdan, Sol. Phys. **203**, 231 (2001).
[17] J. T. Jefferies *et al.*, Sol. Phys. **22**, 307 (1972).
[18] J. T. Jefferies *et al.*, Sol. Phys. **22**, 317 (1972).
[19] S. W. McIntosh, Astrophys. J. **533**, 1043 (2000).
[20] I. J. Craig and J. C. Brown, Astron. Astrophys. **49**, 239 (1976).
[21] I. J. Craig and J. C. Brown, *Inverse Problems in Astronomy: A Guide to Inversion Strategies for Remotely Sensed Data* (Adam Hilger, Boston, 1986).
[22] J. C. Brown, B. N. Dwivedi, P. A. Sweet, and Y. M. Almleaky, Astron. Astrophys. **249**, 277 (1991).
[23] J. C. Raymond and J. G. Doyle, Astrophys. J. **247**, 686 (1981).
[24] C. E. Parnell and P. E. Jupp, Astrophys. J. **529**, 554 (2000).
[25] S. Krucker and A. O. Benz, Astrophys. J. Lett. **501**, L213 (1998).
[26] M. J. Aschwanden, R. W. Nightingale, T. D. Tarbell, and C. J. Wolfson, Astrophys. J. **535**, 1027 (2000).
[27] E. T. Lu and R. J. Hamilton, Astrophys. J. Lett. **380**, L89 (1991).
[28] E. T. Lu, R. J. Hamilton, J. M. McTiernan, and K. R. Bromund, Astrophys. J. **412**, 841 (1993).
[29] L. P. Kadanoff, S. R. Nagel, L. Wu, and S. M. Zhou, Phys. Rev. A **39**, 6524 (1989).
[30] S. D. Edney, P. A. Robinson, and D. Chisholm, Phys. Rev. E **58**, 5395 (1998).

[31] P. A. Robinson, Phys. Rev. E **49**, 1984 (1994).
[32] D. Stauffer and A. Aharony, *Introduction to Percolation Theory*, 2nd. ed. (Taylor and Francis, London, 1994).
[33] D. Berghmans, F. Clette, and D. Moses, Astron. Astrophys. **336**, 1039 (1998).
[34] V. Aletti, M. Velli, K. Bocchialini, G. Einaudi, M. Georgoulis, and J.-C. Vial, Astrophys. J. **544**, 550 (2000).
[35] A. Brković, S. K. Solanki, and I. Rüedi, Astron. Astrophys. **373**, 1056 (2001).
[36] U. Mitra-Kraev and A. O. Benz, Astron. Astrophys. **373**, 318 (2001).
[37] M. J. Aschwanden and P. Charbonneau, Astrophys. J. Lett. (to be published).
[38] H. Isliker, A. Anastasiadis, and L. Vlahos, Astron. Astrophys. **363**, 1134 (2000).
[39] H.-L. Liu, P. Charbonneau, A. Pouquet, T. J. Bogdan, and S. W. McIntosh (unpublished).
[40] H. Isliker, A. Anastasiadis, and L. Vlahos, Astron. Astrophys. **377**, 1068 (2001).